Randomization of gold nano-brick arrays: a tool for SERS enhancement

Yoshiaki Nishijima,[1,*] **Jacob B. Khurgin,**[2] **Lorenzo Rosa,**[3,4] **Hideki Fujiwara,**[5] **Saulius Juodkazis**[3,4]

[1] *Department of Electrical and Computer Engineering, Graduate School of Engineering, Yokohama National University, 79-5 Tokiwadai, Hodogaya-ku, Yokohama 240-8501, Japan*
[2] *Department of Electrical and Computer Engineering, Johns Hopkins University, Baltimore, MD 21218, USA*
[3] *Centre for Micro-Photonics, Faculty of Engineering and Industrial Sciences, Swinburne University of Technology, Hawthorn, VIC 3122, Australia*
[4] *The Australian National Fabrication Facility – ANFF, Victoria node, Faculty of Engineering and Industrial Sciences, Swinburne University of Technology, Hawthorn, VIC 3122, Australia*
[5] *Research Institute for Electronic Science, Hokkaido University, Sapporo 001-0020, Japan*

[*] *nishijima@ynu.ac.jp*

Abstract: Surface enhanced Raman scattering (SERS) was measured on periodic and randomly arranged patterns of Au nano-bricks (rectangular parallelepipeds). Resonant SERS conditions were investigated of a near-IR dye deposited on nanoparticles. Random mixtures of Au nano-bricks with different aspect ratio R showed stronger SERS enhancement as compared to periodic patterns with constant aspect ratio (R varies from 1 to 4). SERS mapping revealed up to ~ 4 times signal increase at the hot-spots. Experimental observation is verified by numerical modeling and is qualitatively consistent with generic scaling arguments of interaction between plasmonic nanoparticles. The effect of randomization on the polarization selectivity for the transverse and longitudinal modes of nano-bricks is shown.

OCIS codes: (160.4236) Nanomaterials; (240.6680) Surface plasmons; (250.5403) Plasmonics; (290.4210) Multiple scattering; (220.4241) Nanostructure fabrication; (310.6628) Subwavelength structures, nanostructures.

References and links

1. J. Suh, C. Kim, W. Zhou, M. Huntington, D. Co, M. Wasielewski, and T. Odom, "Plasmonic bowtie nanolaser arrays," Nano Lett. **12**, 5769–5774 (2012).
2. W. Cai, A. P. Vasudev, and M. L. Brongersma, "Electrically controlled nonlinear generation of light with plasmonics," Science **333**, 1720–1723 (2011).
3. A. E. Miroshnichenko, S. Flach, and Y. S. Kivshar, "Fano resonances in nanoscale structures," Rev. Mod. Phys. **82**, 2257–2298 (2010).
4. A. Kabashin, P. Evans, S. Pastkovsky, W. Hendren, G. Wurtz, R. Atkinson, R. Pollard, V. Podolskiy, and A. Zayats, "Plasmonic nanorod metamaterials for biosensing," Nat. Mater. **8**, 867–871 (2009).
5. T. Kondo, H. Masuda, and K. Nishio, "SERS in ordered array of geometrically controlled nanodots obtained using anodic porous alumina," J. Phys. Chem. C **117**, 2531–2534 (2013).
6. H.-X. Lin, J.-M. Li, B.-J. Liu, D.-Y. Liu, J. Liu, A. Terfort, Z.-X. Xie, Z.-Q. Tian, and B. Ren, "Uniform gold spherical particles for single-particle surface-enhanced Raman spectroscopy," Phys. Chem. Chem. Phys. **15**, 4130–4135 (2013).
7. S. Smitha, K. Gopchandran, N. Nair, K. Nampoothiri, and T. Ravindran, "SERS and antibacterial active green synthesized gold nanoparticles," Plasmonics **7**, 515–524 (2012).
8. F. Lordan, J. H. Rice, B. Jose, R. J. Forster, and T. E. Keyes, "Site selective surface enhanced Raman on nanostructured cavities," Appl. Phys. Lett. **99**, 033104 (2011).

#187794 - $15.00 USD Received 26 Mar 2013; revised 17 May 2013; accepted 19 May 2013; published 29 May 2013

9. K. Ueno, S. Juodkazis, M. Mino, V. Mizeikis, and H. Misawa, "Spectral sensitivity of uniform arrays of gold nanorods to the dielectric environment," J. Phys. Chem. C **111**, 4180–4184 (2007).
10. A. M. Michaels, M. Nirmal, and L. E. Brus, "Surface enhanced Raman spectroscopy of individual rhodamine 6G molecules on large Ag nanocrystals," J. Am. Chem. Soc. **121**, 9932–9939 (1999).
11. D. K. Gramotnev, A. Pors, M. Willatzen, and S. I. Bozhevolnyi, "Gap-plasmon nanoantennas and bowtie resonators," Phys. Rev. B **85**, 045434 (2012).
12. J. Merlein, M. Kahl, A. Zuschlag, A. Sell, A. Halm, J. Boneberg, P. Leiderer, A. Leitenstorfer, and R. Bratschitsch, "Nanomechanical control of an optical antenna," Nat. Photonics **2**, 230–233 (2008).
13. K. Ueno, S. Takabatake, K. Onishi, H. Itoh, Y. Nishijima, and H. Misawa, "Homogeneous nano-patterning using plasmon-assisted photolithography," Appl. Phys. Lett. **99**, 011107 (2011).
14. W. Khunsin, B. Brian, J. Dorfmuller, M. Esslinger, R. Vogelgesang, C. Etrich, C. Rockstuhl, A. Dmitriev, and L. Lern, "Long-distance indirect excitation of nanoplasmonic resonances," Nano Lett. **11**, 2765–2769 (2011).
15. B. Lamprecht, G. Schider, R. T. Lechner, H. Ditlbacher, J. R. Krenn, A. Leitner, and F. R. Aussenegg, "Metal nanoparticle gratings: Influence of dipolar particle interaction on the plasmon resonance," Phys. Rev. Lett. **84**, 4721–4724 (2000).
16. Y. Nishijima, L. Rosa, and S. Juodkazis, "Surface plasmon resonances in periodic and random patterns of gold nano-disks for broadband light harvesting," Opt. Express **20**, 11466–11477 (2012).
17. R.Buividas, L. Rosa, R. Šliupas, T. Kudrius, G. Šlekys, V. Datsyuk, and S. Juodkazis, "Mechanism of fine ripple formation on surfaces of (semi)transparent materials via a half-wavelength cavity feedback," Nanotechnology **22**, 055304 (2011).
18. A. Chou, E. Jaatinen, R. Buividas, G. Seniutinas, S. Juodkazis, E. L. Izake, and P. M. Fredericks, "SERS substrate for detection of explosives," Nanoscale **4**, 7419–7424 (2012).
19. A. K. Sarychev, V. A. Shubin, and V. M. Shalaev, "Anderson localization of surface plasmons and nonlinear optics of metal-dielectric composites," Phys. Rev. B **60**, 16389–16408 (1999).
20. M. I. Stockman, S. V. Faleev, and S. J. Bergman, "Localization versus delocalization of surface plasmons in nanosystems: can one state have both characteristics?," Phys. Rev. Lett. **87**, 167401 (2001).
21. J. B. Khurgin and G. Sun, "Impact of disorder on surface plasmons in two-dimensional arrays of metal nanoparticles," Appl. Phys. Lett. **94**, 22111 (2009).
22. D. J. Bergman and M. I. Stockman, "Surface plasmon amplification by stimulated emission of radiation: Quantum generation of coherent surface plasmons in nanosystems," Phys. Rev. Lett. **90**, 027402 (2003).
23. M. A. Noginov, G. Zhu, A. M. Belgrave, R. Bakker, V. M. Shalaev, E. E. Narimanov, S. Stout, E. Herz, T. Suteewong, and U. Wiesner, "Demonstration of a spaser-based nanolaser," Nature **460**, 1110–1112 (2009).
24. M. Cao, M. Wang, and N. Gu, "Plasmon singularities from metal nanoparticles in active media: Influence of particle shape on the gain threshold," Plasmonics **7**, 347–351 (2012).
25. F. Eftekhari and T. J. Davis, "Strong chiral optical response from planar arrays of subwavelength metallic structures supporting surface plasmon resonances," Phys. Rev. B **86**, 075428 (2012).
26. Y. Nishijima and S. Akiyama, "Unusual optical properties of the Au/Ag alloy at the matching mole fraction," Opt. Mater. Express **2**, 1226–1235 (2012).
27. A. Campion and P. Kambhampati, "Surface-enhanced Raman scattering," Chem. Soc. Rev. **27**, 241–250 (1998).
28. J. R. Lombardi and R. L. Birke, "A unified approach to surface-enhanced Raman spectroscopy," J. Phys. Chem. C **112**, 5605–5617 (2008).
29. S. A. Maier, *Plasmonics: Fundamentals and Applications* (Springer, 2007).
30. S. Juodkazis, L. Rosa, and Y. Nishijima, "Plasmonic solutions for light harvesting in solar and sensing applications," in *Nanoplasmonics: Advanced Device Applications* J. W. M. Chon and K. Iniewski, eds., (CRC Press, 2013), Chap. 3.
31. C. F. Bohren, *Absorption and Scattering of Light by Small Particles* (Wiley Interscience Publication, 1983).
32. J. D. Jackson, *Classical Electrodynamics* (John Wiley & Sons, IIIrd ed., 1998).
33. For example, consider a one-dimensional intensity distribution $I_1(x)$, having constant value 1 for $0 < x < 10$, and a second distribution $I_2(x)$ having value 0.8 for $0 < x < 8$ and 1.8 for $8 < x < 10$. While the two distributions have the same average $\langle I_1 \rangle = \langle I_2 \rangle = 1$, $I_2(x)$ is clearly less uniform than $I_1(x)$. This is reflected in the greater value of the variance estimator $\langle I_2^2 \rangle / \langle I_2 \rangle^2$=1.16 with respect to $\langle I_1^2 \rangle / \langle I_1 \rangle^2$=1. In order to maximize its value the distribution should have a high degree of non-uniformity, which can be slightly increased by mixing nano-bricks with high aspect ratio, while it is the greatest (thus high enhancement) for a random distribution. When R is increased, for the T-mode the non-uniformity is increased and the wavelength decreased, both of which favor an increase in Raman scattering relative to extinction (as the Raman scattering cross-section is proportional to $1/\lambda^4$). For the L-mode, both non-uniformity and wavelength increase, thus the two factors compensate each other, reducing the growth of Raman intensity with R.
34. G. Sun, J. B. Khurgin, and A. Bratkovsky, "Coupled-mode theory of field enhancement in complex metal nanostructures," Phys. Rev. B **84**, 045415 (2011).
35. A. Žukauskas, M. Malinauskas, A. Kadys, G. Gervinskas, G. Seniutinas, S. Kandasamy, and S. Juodkazis, "Black silicon: substrate for laser 3D micro/nano-polymerization," Opt. Express **21**, 6901–6909 (2013).

#187794 - $15.00 USD Received 26 Mar 2013; revised 17 May 2013; accepted 19 May 2013; published 29 May 2013

1. Introduction

The applications of localized surface plasmons originated in metal nano-particles (gold, silver, etc.), are set to be fundamental in several fields of science and engineering research, such as plasmonics and optoelectronics [1–4], and surface enhanced Raman scattering (SERS) spectroscopy [5–10], enabling detection of tiny amounts of substance down to single molecules. In this context, strong importance is given to short-range plasmonic interactions in nanometric-size gaps between close particles [11], which locally produce strong light intensity enhancement [12, 13]. Randomly arranged Au nano-particles can have stronger light enhancement at specific wavelengths, an effect accompanied by the progressive disruption of long-range dipole-dipole interactions [14], as compared with periodically arrayed patterns, where the constant scattering phase delay between first neighbors causes regular extinction peaks with period dependence of wavelength [15].

Recently we have demonstrated such phenomenon experimentally and numerically for random arrays of Au nano-disks [16]. It was found that "hot-spots" where the light field intensity is enhanced up to 2×10^4 (numerically predicted) are found on random patterns, and such values exceed those obtained from periodic nano-disk arrays. By nano-texturing of surfaces through laser ablation, quasi-periodic patterns of ripples are formed [17] with a random distribution of nanoscale features, which are responsible for a strong increase of sensitivity when they are used for Raman sensing [14, 18–20]. How the degree of randomization of the quasi-periodic patterns affects the formation of hot-spots in the spatial and spectral domains, is a topic in need of further investigation [21]. The control of light intensity at the nanoscale can find applications in light harvesting for solar cells, as well as in the medical and bio-sensing fields. Use of randomness in relationship with the particle shape is promising as a way to enhance performance of plasmonic structures, with a view to metal nanoparticle-based spasers [22, 23] and random lasers [24], and to influence chiral effects [25].

Here, we systematically investigated random patterns of Au nano-bricks (rectangular parallelepipeds) of rectangular footprint and of different aspect ratios R ranging from 1 to 4 (where R is the y-size length to x-size width ratio) for surface-enhanced Raman scattering (SERS). SERS mapping was used to experimentally verify the existence of the hot-spots. Numerical modeling of large area patterns of different aspect ratio nano-bricks, for different degrees of randomization, corroborated the experimental observations.

2. Samples and methods

2.1. Fabrication of nano-bricks

The fabrication of the Au nano-brick arrays was carried out by a standard sequence of electron-beam lithography (EBL), Au deposition, and lift-off as previously reported [16, 26]. In short, EBL resist ZEP520A from Zeon was deposited on a glass substrate by spin-coating (3000 rpm for 60 s). After baking at 130°C for 10 min, the resist surface was coated with a charge dissipating agent. EB drawing was carried out using 50 kV acceleration voltage on an EBL system ELS 7500EX from Elionix. After developing in ZEP-RD from Zeon for 1 min, and rinsing in ZMD-B for 15 s twice, 2 nm of Cr and 65 nm of Au were deposited using a thermal vacuum evaporation system from ULVAC. Finally, lift-off was performed in a resist remover ZDMAC from Zeon, then the sample was rinsed in acetone and methanol.

The randomness of nano-bricks was controlled by performing random-walk steps of $s =$ 100 nm starting from the initial periodic square pattern of nano-bricks with period $\Lambda = 600$ nm. The randomness coefficient, R_{an}, corresponds to the number of random-walk steps, e.g. $R_{an} = 6$ defines a pattern where the maximum possible separation of a particle from its initial position (in a periodic setting) is 600 nm. To prevent the nano-bricks from overlapping during the ran-

#187794 - $15.00 USD Received 26 Mar 2013; revised 17 May 2013; accepted 19 May 2013; published 29 May 2013

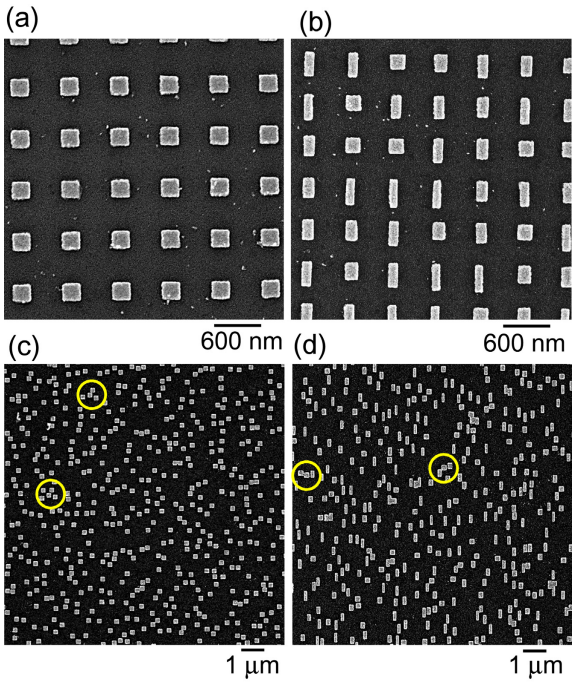

Fig. 1. SEM images of periodic arrays of nano-bricks of different aspect ratio R: (a) constant $R = 1$ and (b) mixture of $R = 1$ to 4. Randomly arranged nanobrick arrays with (c) constant $R = 1$ and (d) mixture of R from 1 to 4. Randomization degree $R_{an} = 6$ corresponds to 6 random-walk steps of 100 nm each, and circles mark closely-clustered nano-bricks, where the strongest light enhancement occurred (see text for details).

dom walk, a CAD design rule defined 10 nm as their smallest allowed separation, both for constant and mixed aspect ratio. The 2D Fast Fourier transform (2D-FFT) of the CAD pattern and the SEM images showed recognizable periodic features (periodic spots in the FFT map) up to a randomness of $R_{an} = (3-4)$, a result similar to our previous study [16].

2.2. Raman scattering and extinction spectral characterization

Raman scattering was measured using a Raman microscope inVIA from Renishaw Co. for an excitation wavelength of 785 nm. Steady-state measurements were carried out with a $20\times$ objective lens, having a spot of $100 \times 5\ \mu m^2$ cross-section. For the Raman mapping the spot size was $\sim 3\ \mu$m. A laser dye IR-26 from Exciton, Inc was used as a probe, as it has a broad absorption bandwidth in the near-IR region. The 785 nm excitation was realized through resonant Raman excitation. The fabricated samples with Au nano-bricks were dipped into a 1 mM IR-26 methanol solution. After immersion for more than 12 hours, the samples were washed in pure methanol, dried, then the SERS emission of IR-26 was measured.

The structures were imaged with a scanning electron microscope (SEM) JSM-7500F from JEOL and the transmission spectra were measured with a confocal microscope system, composed of a microscope and an optical spectrum analyzer in the near-IR region, Q8381A. A $10\times$ objective lens of $NA = 0.5$ with a confocal pinhole of 0.1 mm diameter was set in an Optiphoto microscope from Nikon.

#187794 - $15.00 USD Received 26 Mar 2013; revised 17 May 2013; accepted 19 May 2013; published 29 May 2013

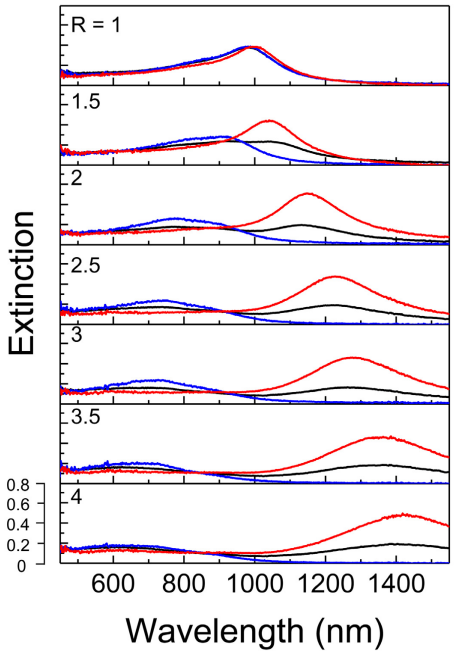

Fig. 2. Extinction spectra of the periodic array of nano-bricks with aspect ratio from 1 to 4, with the indicated light polarization. The L- and T-modes are shown together with the non-polarized light measurement (black line). Extinction scale is the same for all patterns.

2.3. Finite difference time domain simulations

Numerical modeling of light enhancement on a large area of nano-bricks was carried out with the 3D-FDTD method implemented with the Lumerical software from FDTD Solutions. The substrates were modeled as glass layers on which the gold nano-bricks were placed according to the layout and dimensions specified in the CAD pattern file, which was imported for the calculations. The refractive index spectra of the materials were fitted from the experimental values obtained in literature, by means of a built-in polynomial model.

To obtain reasonable use of computational resources without sacrificing accuracy, a section of the substrate of 11×11 periods was modeled, included in a FDTD domain closed in all directions by perfectly matched layers (PMLs) to avoid spurious reflections. A central area of 5×5 periods was illuminated by a total-field scattered-field (TFSF) source, to measure separately the total field in the central area, and the field scattered outside. This also increases PML efficiency, as it only has to absorb the weaker scattered field instead of the total one. The simulated layouts are: (i) regular array $R_{an} = 0$ of 600 nm period of regular square nano-bricks of 200×200 nm ($R = 1$), (ii) random array $R_{an} = 6$ of regular nano-bricks, (iii) regular array of mixed aspect ratio nano-bricks (R from 1 to 4), and (iv) random array of mixed nano-bricks. In the cases (ii) and (iv), since the nano-bricks cannot cross the TFSF source boundary lest simulation accuracy is compromised, their position is slightly adjusted; this does not influence the modeling results significantly due to the large total number of nano-bricks inside the simulation domain.

The simulations were performed on the swinSTAR supercomputer at Swinburne University, having nodes of 16 cores and 64 GB memory each. The memory footprint was around 200 GB and took about 6 hours to run on a 16-node cluster for a total of 256 cores.

#187794 - $15.00 USD Received 26 Mar 2013; revised 17 May 2013; accepted 19 May 2013; published 29 May 2013

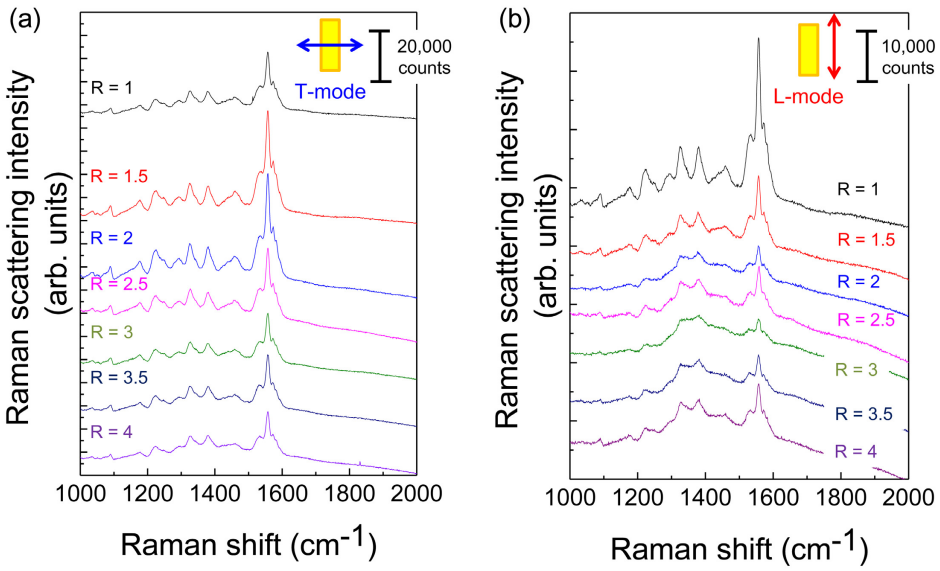

Fig. 3. Experimental SERS spectra of IR-26 adsorbed on gold nano-bricks of periodic pattern but different aspect ratio *R*. Note the difference in the vertical scale between the panels.

3. Results

3.1. Extinction and SERS of periodic and random patterns

We fabricated 65-nm-tall Au nano-bricks in order to recover a better shape closer to the designed rectangular cross-section. Figure 1 shows SEM images of Au nano-bricks with different aspect ratios and of their random mixtures. The volume of the Au nano-bricks was kept constant for each aspect ratio, with a 600 nm period for the periodic arrays. In the random patterns, some nano-bricks are adjoined, since the 10 nm separation enforced in the CAD pattern could not be exactly reproduced in the fabricated patterns.

Figure 2 shows the experimental extinction spectra of the nano-bricks of constant aspect ratio variable from 1 to 4. With increasing aspect ratio, the longitudinal L-mode resonance wavelength red-shifts while the transversal T-mode blue-shifts. Since the volume of the Au nano-bricks is kept constant, a narrowing of the width causes an expected blue-shift of the T-mode, and likewise the longer rods show a red-shift of the L-mode. The geometry of nano-bricks and patterns were chosen to have extinction maxima in the near-IR spectral region, where the dye SERS measurements were carried out.

First, periodic patterns of constant aspect ratio nano-bricks were investigated. Figure 3 shows the Raman scattering spectra of the IR-26 laser dye adsorbed on the Au nano-bricks. Strong Raman peaks specific to IR-26 appeared from 800 to 1600 cm^{-1}. The absolute value of the Raman intensities varies for each pattern and follows the extinction values. The SERS signal shows electromagnetic and chemical enhancements: the electromagnetic effect closely follows the extinction spectrum. Therefore, by normalizing the SERS signal to extinction at the excitation and Raman scattering wavelengths, it is possible to unveil other field enhancement or quenching contribution, if present. This is important, since the intricacies of SERS enhancement are still strongly debated in literature [27, 28].

The normalized SERS intensity at 1558 cm^{-1} is shown in Fig. 4 for patterns of different aspect ratio. The experimentally measured SERS intensity is divided by the extinction value at the irradiation and Raman scattering wavelengths. Then, it is normalized to the SERS intensity

#187794 - $15.00 USD Received 26 Mar 2013; revised 17 May 2013; accepted 19 May 2013; published 29 May 2013

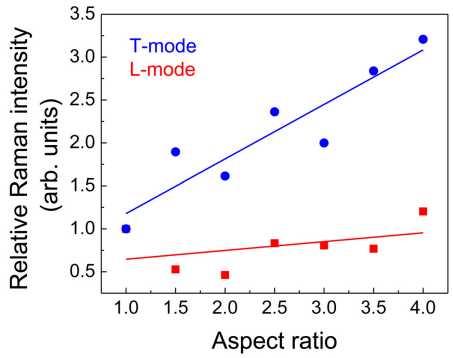

Fig. 4. Normalized SERS signal as a function of aspect ratio R for the periodic patterns. The SERS signal was normalized to the extinction values at the excitation and Stokes 1558 cm^{-1} wavelengths; then, the value was further normalized to the SERS signal obtained on a periodic square (aspect ratio $R = 1$) pattern.

value of the periodic square nano-brick structures ($R = 1$). Such normalization is expected to bring out the effect of SERS contributions from hot-spots, since the spectrally narrow and strongly spatially localized light field enhancement is averaged in the extinction measurements. The intensity of the T-mode has a tendency to increase with the aspect ratio, however the L-mode is almost constant or somewhat decreased as compared with the periodic $R = 1$ pattern. This behavior is understandable from the analysis of the extinction spectra shown in Fig. 2. The local field factor is proportional to the extinction at the wavelengths of excitation and scattering. The local E-field at the hot-spots (edges or/and gaps) shows an electromagnetic enhancement factor $L(\nu) = |\mathbf{E}_{loc}(\nu)|/|\mathbf{E}_0|$, where $\mathbf{E}_0$ is the incident light E-field amplitude. The SERS scattered power is given as [29]:

$$P_s(\nu_s) = N\sigma_{SERS}L(\nu_l)^2L(\nu_s)^2I(\nu_l), \tag{1}$$

where the field enhancements at the excitation and Raman scattering wavelengths (frequency $\nu_{l,s} = c/\lambda_{l,s}$) are considered; here N is the number of scatterers, σ_{SERS} is the SERS scattering cross-section, I is the irradiation intensity. Since usually the laser and Raman wavelengths are similar, the total enhancement factor is assumed to be $R \equiv L(\nu_l)^2L(\nu_s)^2 \simeq |\mathbf{E}_{loc}|^4/|\mathbf{E}_0|^4$. However, as shown in Fig. 2, this rule cannot be used when there are considerable extinction variations. This is also a very important factor for measurement of local temperature in nano-gaps, from the ratio of Stokes to anti-Stokes Raman peaks, where the SERS signal has to be normalized to extinction at the excitation and Raman scattering wavelengths [30].

Next, SERS on random arrays of nano-bricks was investigated. A random mixture of structures with aspect ratios varying from 1 to 4 was fabricated for SERS. Typical extinction spectra are shown in Fig. 5. Periodic (randomness $R_{an} = 0$) nano-square structures show spectral broadening of the extinction peaks with increasing randomness. Due to nanoparticle symmetry, the extinction has no polarization dependence. In the case of nano-bricks, which originally have a polarization dependence of extinction when their aspect ratio $R > 1$, the polarization dependence persists with pattern randomization and shows broadening (Fig. 5).

The cumulative effect of randomness R_{an} and aspect ratio R of nano-brick patterns for SERS intensity is summarized in Fig. 6, where the resonant Raman spectra are presented, normalized by extinction at excitation (785 nm) and Raman scattering (894 nm corresponding to 1558 cm^{-1}) wavelengths. The Raman intensity of the 1558 cm^{-1} peak shows dependence on both R_{an} and R. Interestingly, SERS intensity increased with increasing randomness for both

#187794 - $15.00 USD Received 26 Mar 2013; revised 17 May 2013; accepted 19 May 2013; published 29 May 2013

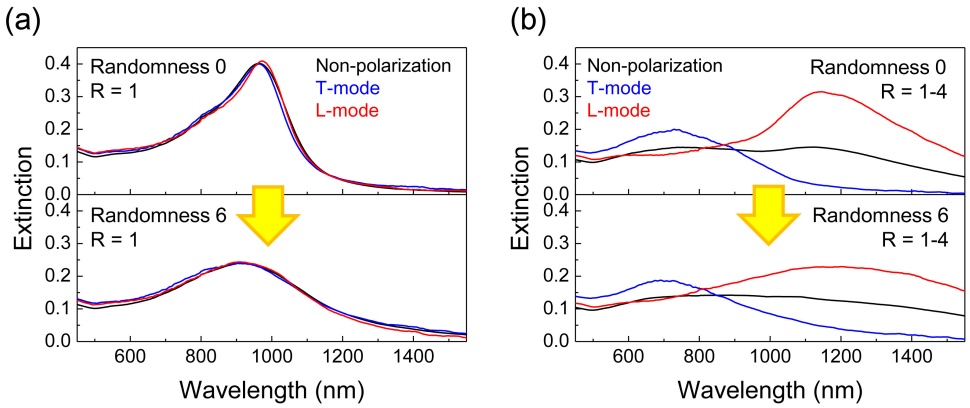

Fig. 5. Polarization dependence of the extinction spectra for the periodic (top-row) and random $R_{an} = 6$ (bottom-row) arrangements of (a) square nano-bricks, and (b) nano-bricks with aspect ratio varying from $R = 1$ to 4.

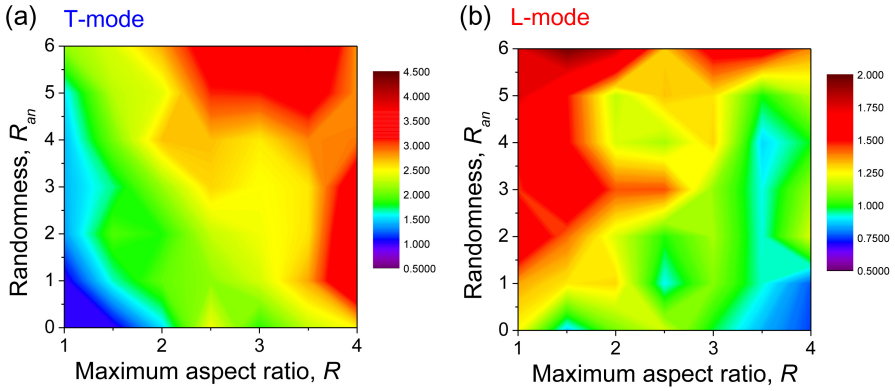

Fig. 6. SERS intensity maps of the major 1558 cm^{-1} Raman mode. On the vertical axis is the randomness $R_{an} = 0$ (periodic) to 6 and on the horizontal one is the maximum aspect ratio of the pattern, from $R = 1$ (squares) to 4 (seven different patterns changing in steps of 0.5, see Fig. 5. The plots show the polarization dependence of (a) L-mode and (b) T-mode.

the L- and T-mode. The experimentally observed enhancement reached $4\times$ for the T-mode. Randomization with $R_{an} = 6$ gave a $2\times$ enhancement as compared with periodic patterns of $R = 1$ and $R_{an} = 0$. This is in good agreement with numerical simulations presented in Sec. 3.2.

This additional enhancement is due to hot-spot formation as a result of pattern randomization, as we recently showed [16]. SERS mapping was carried out on patterns of different aspect ratio and randomization coefficient. The spot diameter and stepping distance were $\sim 3\ \mu$m. Results for periodic and random patterns are shown in Fig. 7. All samples were measured for T-mode excitation, to have a better comparison between different patterns at the excitation wavelength.

In the case of periodic structures with nano-bricks of the same aspect ratio, the SERS maps were flat over the fabricated $100 \times 100\ \mu m^2$ region (Fig. 7). The average SERS count rate was approximately 2000 with a min-to-max span of ± 100. When different aspect ratio nano-bricks were mixed, weak hot-spot-like spikes began to emerge. This is due to the broken periodicity due to nano-bricks of different widths, however this did not affect the overall average, but rather

#187794 - $15.00 USD Received 26 Mar 2013; revised 17 May 2013; accepted 19 May 2013; published 29 May 2013

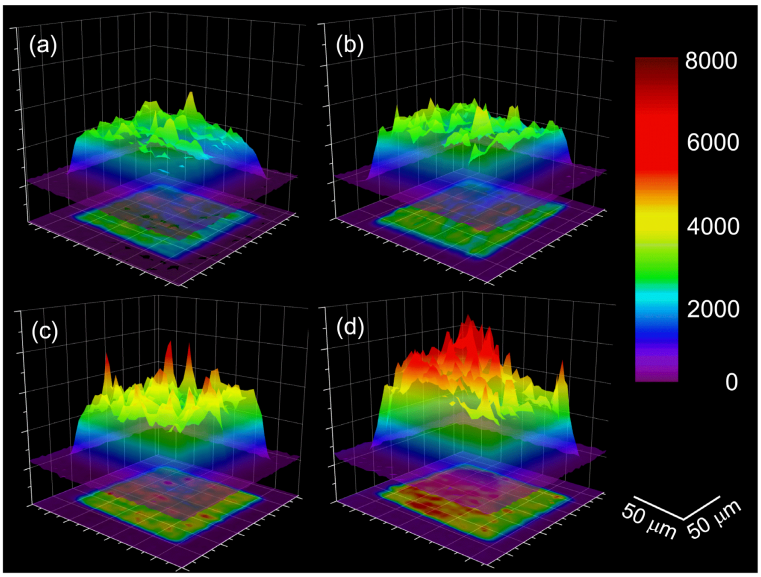

Fig. 7. SERS mapping at the 1558 cm^{-1} Raman wavelength for (a) periodic pattern with $R = 1$, (b) periodic pattern with mixture of $R = 1$ to 4, (c) random pattern with $R = 1$, and (d) random pattern with mixture of $R = 1$ to 4. The random pattern has randomness $R_{an} = 6$. Note that for all panels the SERS intensity scale is the same from 0 to 8000; the footprint of the SERS region was $100 \times 100\ \mu m^2$.

the min-to-max span, which increased to ± 500.

The pattern randomization had a stronger effect on the average SERS intensity and the spikes which follow the surface distribution of the hot-spots. This is the experimental evidence of hot-spot formation due to randomization. The strongest SERS was observed on the patterns which are fully randomized and have the widest range of nano-bricks of different aspect ratios. It is obvious that stronger enhancement occurred between bricks separated by few nanometers. The excitation spot areas ($\phi \sim 3\ \mu m$) interrogates $20 \sim 30$ nanoparticles and the Raman intensity is averaged, however, we can clearly recognize the high intensity spot by mapping. The Raman mapping method is useful for searching the regions where hot-spots are formed. The average SERS count rate was approximately $\sim$2500 with maxima $\sim$1000 counts higher. Next, the experimentally observed trends are numerically corroborated by 3D finite-element time-domain (3D-FDTD) simulations.

3.2. Numerical simulations of field enhancement

The numerical results are shown in Fig. 8, where the calculated extinction cross-sections show similar behaviors as the experimental ones in Fig. 5. Simulated nano-bricks have exact shape; when the experimental extinction of 0.4 is normalized to a numerical cross-section of 10 calculated on a 25-brick cluster and normalized the the total gold area in the cluster, differences can be safely attributed to fabrication tolerances. In particular, the slight difference between L- and T-mode for layout (ii) all but disappears in the experiment, while in layout (iii) and (iv) the randomization broadening is less pronounced in the simulation. In the latter case, the T- and L-mode peaks are slightly blue-shifted in the experiment, suggesting that the fabricated nano-bricks are actually smaller, possibly due to fabricated corners being rounded.

The SERS intensity has been estimated from the calculated field enhancement and cross-

#187794 - $15.00 USD Received 26 Mar 2013; revised 17 May 2013; accepted 19 May 2013; published 29 May 2013

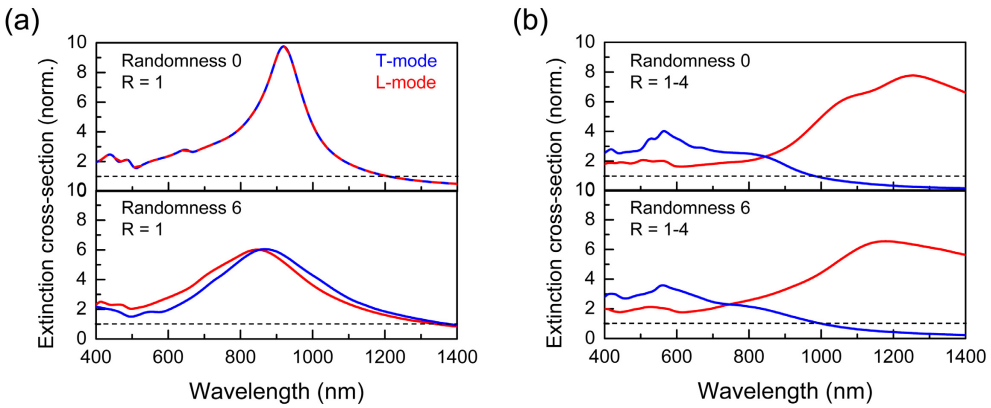

Fig. 8. Extinction cross-sections numerically calculated for the periodic (top-row) and random $R_{an} = 6$ (bottom-row) arrangements of a 25-element cluster of (a) square nano-bricks, and (b) nano-bricks with aspect ratio varying from $R = 1$ to 4. The cross-sections are normalized to the total geometrical area of the gold in the cluster (black dashed line).

sections at the excitation and Raman wavelengths for the L- and T-mode, according to the layouts (i) to (iv), which correspond to the four corners of the panels in Fig. 6. For the T-mode the trend is clearly confirmed as, where the normalized value is 1 for layout (i), for layout (ii) it is 9× (2× experimental), for (ii) it is 6× (2.5× exper.), and for (iv) it is 10× (4.5× exper.). The simulated results for the T-mode are 2∼3 times higher than the experimental ones, this is influenced by the numerically perfect definition of corners and interfaces, giving results that can be considered upper performance bounds for a finely tuned fabrication process.

Figure 9 shows the field enhancement distributions for the best-case T-mode (layout (iv) and L-mode (layout (ii)), as compared with layout (i) at the Raman scattering wavelength of 894 nm. The top panels show the field cut in the *xy*-plane flush with the top of the nano-bricks, while the bottom panels show the field cut in the vertical plane crossing the centre of the array and parallel to the excitation polarization. The square box shows the total-field region encompassing the 25 nano-blocks on which the cross-sections are calculated, while outside of it the scattered field is visible. The plots for layout (i) in Fig. 9 (a,d) show a wide distribution of the long-range coupled optical energy, insensitive to the *x* or *y* polarization direction, for a maximum field enhancement of 7×10^3 on the top of the nano-bricks, when extinction cross-section values are taken into account. This climbs to 7.1×10^4 for the T-mode on layout (iv) in Fig. 9 (b,e), where the scattering appears short-ranged and asymmetrical; the vertical-plane cut shows how the few hot-spots corresponding to nano-bricks very close to each other scatter very strongly both in air and in the substrate. This is true to an extent also for the L-mode on layout (ii) in Fig. 9 (c,f), where the adjusted enhancement reaches 4.2×10^3.

4. Discussion

The spectra shown in Fig. 2 can be modeled theoretically by harmonic oscillators whose dissipation rate as a function of dispersion can be written as $\alpha_{L,T} \sim \gamma(\omega)/[(\omega - \omega_{L,T})^2 - \gamma^2(\omega)]$, where the resonant frequencies $\omega_{L,T}$ are determined mostly by geometry, and the scattering rate γ is strongly frequency-dependent. The longitudinal resonance always has lower resonant frequency decreasing with increase in aspect ratio *R*, as the longitudinal electric field gets progressively less contained inside the metal nano-bricks, and the restoring force driving the oscillation decreases. Similarly, the transverse resonance is always blue-shifted relative to the

#187794 - $15.00 USD Received 26 Mar 2013; revised 17 May 2013; accepted 19 May 2013; published 29 May 2013

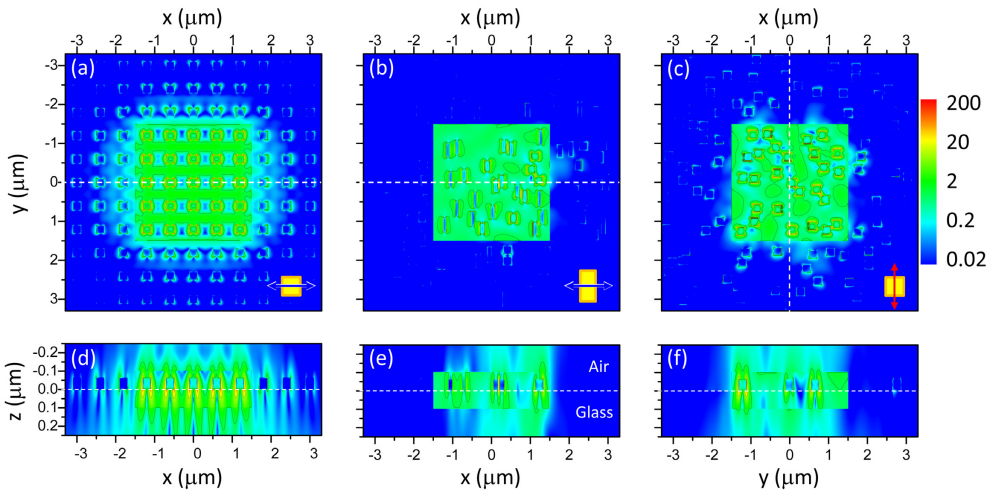

Fig. 9. E-field intensity enhancement log-scale maps numerically calculated for (a,d) periodic layout (i) as compared with the highest enhancement condition for (b,e) T-mode (random layout (iv) and (c,f) L-mode (random layout (ii). The field sections are (top) *xy*-plane flush with the top of the nano-bricks and (bottom) vertical plane crossing the array center and parallel to the excitation polarization. The white dashed lines show (top) the position of the vertical plane sections and (bottom) the glass-air boundary. The box shows the total-field region, while outside the scattered field can be seen. Contour lines show constant intensity enhancement (1 for dark green, 10 for dark yellow).

longitudinal one, because the transverse field tends to get progressively more contained inside the metal, thus increasing the restoring force. The resonant frequencies can be reasonably well fitted using a rough analytical model for the ellipsoid from [31] to estimate the depolarization factors $N_{L,T}$, and then use the data for the real part of the dielectric constant of gold $\varepsilon_r(\omega)$ from [32] to obtain the resonant frequencies from the equation:

$$N_{L,T}[\varepsilon_r(\omega_{L,T}) - 1] = 1. \tag{2}$$

The fact that the imaginary part of the gold dielectric constant $\varepsilon_i(\omega)$, and hence the damping rate, increases rapidly at wavelengths shorter than 700 nm, as well as the increase of radiative loss proportional to ω^2, leads to a strong asymmetry of the extinction spectra, with a pronounced shelf in the short wavelength region, as well as a general suppression of the transverse peak relative to the longitudinal one. The spectra also appear not fully Lorentzian and that comes from the dipole-dipole coupling between the particles. Following the theory of [21], we estimate the broadening imposed by dipole coupling to be about $\Delta\omega_{L,T} \sim \omega_{L,T}(d/a)^3 \sim 0.03\omega_{L,T}$, where d is the distance between the nano-bricks and a is their characteristic dimension. This broadening due to coupling (or one can say plasmon tunneling between the particles) thus amounts to about 30 nm, compared to the broadening due to damping $\gamma(\omega)$ that is much larger, on the order of 100-150 nm; hence, one can consider most surface plasmons to be localized on either one or maybe two particles, even in the absence of disorder which would cause even farther localization. But also, as our previous work [34] has shown, there can be a few delocalized modes in which the resonant energy transfer can lead to the formation of hot-spots in which the field gets concentrated.

Figure 4 shows an interesting result as the ratio of Raman intensity to the square of intensity enhancement grows with the increase of aspect ratio R for the transverse polarization, while such a striking difference in the normalized spectra can be explained by the fact that total

#187794 - $15.00 USD Received 26 Mar 2013; revised 17 May 2013; accepted 19 May 2013; published 29 May 2013

extinction is proportional to the integral of $\int_{Metal}|E_{loc}|^2/|E_0|^2 dV$ over the fraction of SPP mode inside the metal, where the electrons that actually dissipate the energy (both radiatively and non-radiatively) are located, while Raman intensity is proportional to $\int_{Dye}|E_{loc}|^4/|E_0|^4 dV$ (the integral is over the volume of SPP mode where the dye molecules are located). The ratio plotted in Fig. 4 is then proportional to $\int_{Dye}|E_{loc}|^4 dV/\left(\int_{Metal}|E_{loc}|^2 dV\right)^2$ and tends to increase for more uneven distribution of electric field, which is the feature of transverse modes at larger R, as the energy tends to concentrate near the corners.

Consider that, if $I(x,y,z)$ is the local E-field intensity, the normalization of Fig. 4 corresponds to evaluating the ratio $\langle I(x,y,z)^2\rangle/\langle I(x,y,z)\rangle^2$, which in essence measures the non-uniformity of the intensity distribution by building an estimator of its variance as a stochastic process and normalizing it by its average [33].

In Fig. 5(a) one can see the extinction spectrum variation caused by the randomness. According to [21], the strong randomness value of 6 (Fig. 1(c)) cannot be treated as a small perturbation – but its impact can nevertheless be quickly estimated by observing that it is the relatively large number of pairs of nano-bricks that nearly touch each other, that experience the largest shift of their resonance frequencies, on the order of $\Delta\omega_{L,T} \sim \omega_{L,T}(a/2a)^3 \sim \omega_{L,T}/8$, which makes this coupling-induced broadening comparable to the original damping-induced broadening. As a result, the spectra at the bottom differ dramatically from those at the top. When it comes to the impact of randomness on the extinction spectrum of the mixed nano-bricks in Fig. 5(b), the impact of disorder in placement is about the same as disorder in shape, that already broadens the upper Fig. Hence, the difference between the lower and upper Figs. is not as large as in Fig. 5(a).

Raman enhancement is shown in Fig. 6. It is clear that the normalized Raman efficiency increases with randomness for both L- and T-modes, but in a different fashion. For both modes, one can identify the enhancement with the hot-spots that occur wherever the nicely coupled dimer or trimer is formed. Then, as shown in ref. [34], first the dipole mode of a larger nanobrick get excited with field enhancement of as much as Q-factor of the mode ($Q \simeq 5$ in this work). Following that the energy get resonantly transferred to smaller nanobricks and then to narrow gaps between them. Each time excitation is transferred to the dipole mode of a smaller particle or to the gap mode the field gets additional enhancement by a factor of Q. Since the Raman enhancement is proportional to the fourth power of the field, one can easily see that it can be as high as $Q^{12} \sim 2\times 10^8$ or higher. All in all, it is rather difficult to predict in advance which cluster will offer larger enhancement, hence by randomization we greatly increase the chance of getting just the right combinations for the hot-spots, as shown in the circles Fig. 1. Now, when it comes to elongated nano-bricks, statistically there is higher probability for them to align in a way to form a smaller gap for the T-mode than for the L-mode – therefore, for the T-mode the largest Raman enhancement takes place for larger R, while for the L-mode it is the $R = 1$ square nano-bricks that have the strongest Raman enhancement.

As one can see from the experimental data in Fig. 7 and the numerical results of Fig. 9, the hot spots are not distributed uniformly over the surface, and the highest density of them is indeed found when one has non-uniform distribution of both shapes and positions of the nano-bricks, resulting in the highest probability of having a local arrangement of bricks that is most favorable for field enhancement, such as dimers and trimers with narrow gaps between them. These results indicate that designing optimum SERS substrates is a far from trivial process, and perhaps randomization and disorder offer a good route to achieve a good performance, which may not be the best theoretically possible result, but is the one that can be reliably achieved.

#187794 - $15.00 USD Received 26 Mar 2013; revised 17 May 2013; accepted 19 May 2013; published 29 May 2013

5. Conclusions

In this study, we experimentally observed resonance SERS enhancement induced by randomization of nano-brick patterns. The SERS intensity increased approximately twice when nano-bricks of different aspect ratios were intermixed. An additional 4 times enhancement was observed by randomization of periodic patterns. Formation of strongly localized hot-spots was confirmed by SERS mapping and by 3D-FDTD simulations. The observed SERS enhancement is consistent with spectral and spatial localization of light field induced by randomization [21, 34]. Fabrication of random nano-patterns and nano-textured surfaces usually requires less elaborated fabrication techniques, e.g., dry plasma etching for nano-textured Si [35], and favors practical applications in harvesting of solar energy and in bio-/medical sensing.

Acknowledgments

YN gratefully thanks Prof. Toshihiko Baba from Yokohama National University for fruitful discussions and granting access to fabrication and characterization facilities. This work was financially supported by the Research Foundation for Opt-Science and Technology. SJ is grateful for support via Australian Research Council DP130101205 project. Part of this work was performed on the swinSTAR supercomputer at Swinburne University of Technology.

#187794 - $15.00 USD Received 26 Mar 2013; revised 17 May 2013; accepted 19 May 2013; published 29 May 2013